Constant-pH molecular dynamics simulations of progressive activation in a proton-gated ion channel

Anton Jansen[1], Paul Bauer[1], Rebecca J. Howard[1,2], Berk Hess[1], and Erik Lindahl[1,2,*]

[1]Science for Life Laboratory & Swedish e-Science Research Center, Department of Applied Physics, KTH Royal Institute of Technology, PO Box 1031, SE-171 21 Solna, Sweden
[2]Science for Life Laboratory, Department of Biochemistry and Biophysics, Stockholm University, PO Box 1031, SE-171 21 Solna, Sweden
[*]Corresponding author: erik.lindahl@scilifelab.se

Abstract

Allosteric activation of ligand-gated ion channels is critical to electrochemical signal transduction, yet the details of how structural transitions are induced remain unclear. The proton-gated *Gloeobacter violaceus* ligand-gated ion channel (GLIC) offers an invaluable model system to study this process, and with high-resolution structures available it should in principle be possible to approach computationally. However, molecular dynamics has traditionally struggled to accurately describe numerous dynamic protonation states with scalable efficiency. Here, we employ a new constant-pH method to simulate GLIC at resting and activating pH, starting from closed and open structures. Our simulations identify E26 and E35 as early protonation sites in gating, and reveal state-dependent shifts in pKa at multiple residues, as well as side chain and domain rearrangements supporting a progressive activation mechanism. Our results demonstrate the applicability of constant-pH simulation to substantiate detailed activation mechanisms in a multidomain membrane protein, likely extensible to other complex systems.

Significance statement

Electrostatic interactions play important roles in protein structure and function. Since changes in pH will (de)protonate residues and thereby modify such interactions, pH itself is a critical environment parameter. However, protonation states of titratable residues are static during classical molecular dynamics simulations. Recently, a *constant-pH* algorithm was implemented in the GROMACS package, allowing pH-effects to be captured dynamically. Here, we used this implementation to perform constant-pH simulations of a proton-gated ion channel, providing insight into its activation mechanism by revealing state-dependent shifts in protonation as well as pH-dependent side chain and domain-level rearrangements. The results show that constant-pH simulations are both accurate and capable of modeling dozens of titratable sites, with important implications e.g. for drug design.

Introduction

Pentameric ligand-gated ion channels (pLGICs) comprise a family of transmembrane receptors mediating electrochemical signal transduction in a variety of animal cell types [1]. These channels play an especially important role in the nervous system, where they alter the membrane potential upon binding of neurotransmitters. Their involvement in neurotransmission pathways has led to concerted efforts to understand the structure and function of pLGIC sub-families, with several structures now available from X-ray diffraction and cryogenic electron microscopy (cryo-EM) to guide experimental and theoretical studies [2].

One channel that has been of particular interest is the homopentameric bacterial *Gloeobacter violaceus* ligand-gated ion channel (GLIC) (Fig. 1A). Similar to some other bacterial channels where the eukaryotic

homologs might be sensitive to voltage or neurotransmitters [3], GLIC is gated by a change in pH, with the channel opening under acidic conditions. This pH-gated channel has served as a model system for the pLGIC family [4], with a multitude of open and closed structures resolved, both in the presence and absence of various ligands and mutations [5–16]. It has also been the subject of multiple computational studies [17–25] to better understand both the gating transition and allosteric modulation.

Structurally, the GLIC channel assembles as a pentamer that consists of an extracellular domain (ECD) and a transmembrane domain (TMD). The ECD comprises β-strands β1-β10, with loops A-F forming a canonical ligand-binding pocket. The TMD comprises α-helices M1-M4, with the M2 helices of each subunit providing the lining for a central ion-conducting pore. Compared to the closed state, the open state of GLIC is characterized by a rigidified and contracted ECD and an expanded transmembrane pore (Fig. 1C). More precisely, the gating transition is believed to proceed from a counter-clockwise rotation of the ECD relative to the TMD (ECD twist), to a contraction between intrasubunit β sheets (β-expansion), and then to a transition of the outward-facing portion of M2 towards the neighboring M1 helix (M2-M1(-) distance) [22]. Extensive experimental efforts have been invested to identify the site responsible for gating, including full mutational mapping of all Asp, Glu and His residues in combination with electrophysiology[21], but interestingly it has not been possible to assign the gating process to a single titratable site. Instead, the channel pore opening is believed to be driven by an ensemble of protonation events including the pH-sensitive residues E35 and E243 [21–24] (Fig. 1D). Still, a complete molecular picture of the proton-gating transition of GLIC remains lacking.

A prominent problem when studying pH-dependent conformational change is that experimental techniques such as X-ray crystallography and cryo-electron microscopy (cryo-EM) lack the resolution required to determine the protonation state (i.e. microscopic pKa) of titratable residues. This problem is not limited to GLIC, but applies to pH-dependent macromolecular systems in general. Even with methods such as neutron diffraction that theoretically can resolve protons [26], the local electrostatic environment in a crystal or on a grid is not guaranteed to correspond to the cellular environment. Given these experimental limitations, computational methods such as molecular dynamics (MD) simulations may provide deeper insight. Although MD is able to capture a variety of both intra- and intermolecular interactions with high precision, traditional simulations typically do not allow for an explicit value of environmental pH. It is generally not possible to model the dynamics of changing protonation states without resorting to quantum mechanics-based approaches that allow for explicit bond formation and breaking, but these are prohibitively slow and presently orders-of-magnitude away from the time scales of large conformational changes in membrane proteins.

Over the years, significant efforts have been invested in capturing pH-dependence in MD simulations in a more realistic fashion [27–51]. To avoid hysteresis effects where the structure adapts to and stabilizes the initially chosen protonation states, some of these *constant-pH* molecular dynamics (CpHMD) methods are based on the concept of λ-dynamics [52] (Fig. 1B). In this approach, a virtual one-dimensional λ-coordinate is introduced for every titratable site and integrated together with the positions of regular atoms. Each λ-coordinate can move continuously between 0 and 1, with 0 corresponding to the protonated, and 1 corresponding to the deprotonated state. The charge on the titratable residue is then coupled to the movement of the λ-coordinate, which in turn evolves on a potential specifically chosen as to capture the pH-dependence of the associated residue [50].

Using CpHMD methods to study ion channels such as GLIC can be challenging: GLIC contain 185 titratable sites, there is not one specific residue responsible for the gating transition [23], and shifts in protonation are often subtle. However, a new λ-dynamics method recently implemented in GROMACS [53] makes it possible to run constant-pH simulations of an arbitrary number of titratable residues, while still achieving the performance required for sampling at the relevant time scales necessary to explore biological function [50, 51]. This implementation features a fully-consistent particle mesh Ewald (PME) treatment of long-range electrostatics for both the regular atoms and the λ-coordinates, a multisite representation for histidine (His) residues, and the inclusion of non-interacting buffer particles to maintain a net-neutral system during the simulations. The latter is required for preventing PME artifacts [54]. In the present work, we show how this CpHMD implementation can be used to perform fully titratable CpHMD simulations of a large membrane protein such as GLIC in multiple states and conditions, and that it makes it possible identify both selective stabilization and early protonation sites in the GLIC pH-driven gating process.

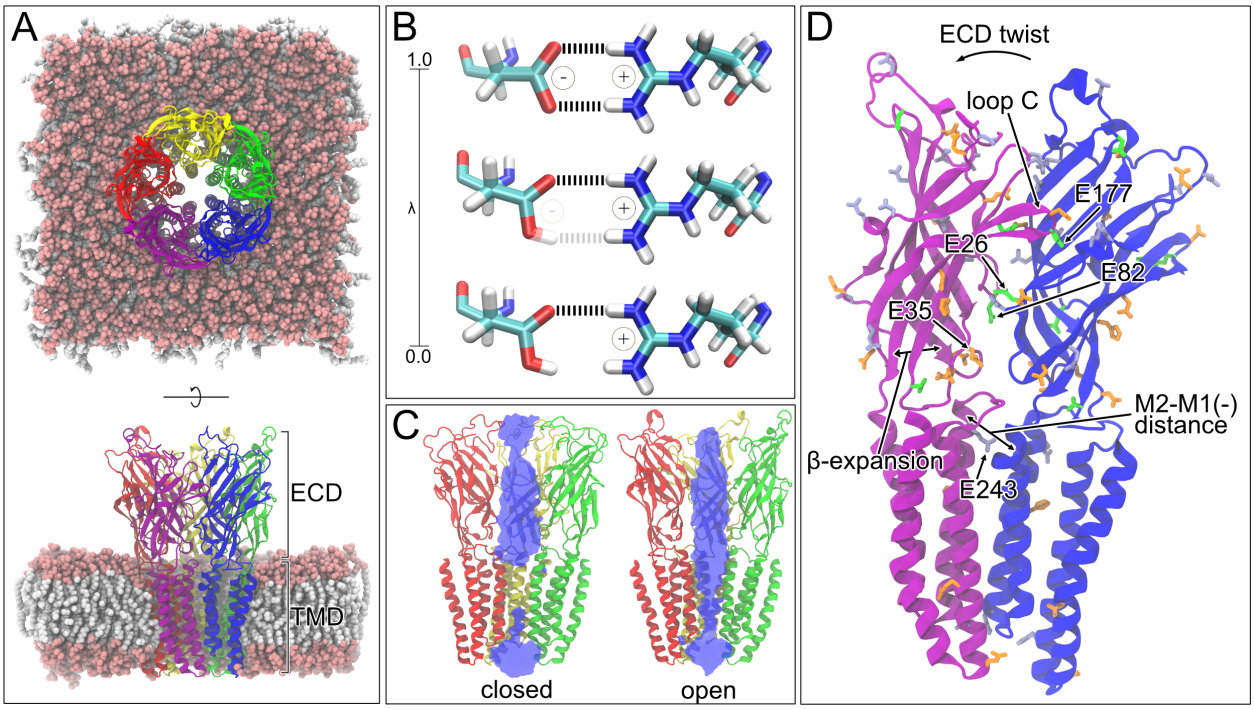

Figure 1: Overview of GLIC structure and CpHMD methodology. (A) Top and side view of the GLIC open state embedded in a lipid bilayer, with the ECD and TMD regions indicated. **(B)** Schematic of λ-dynamics based CpHMD for an aspartic acid. Each titratable residue is coupled to a 1D λ-coordinate. As the λ-coordinate changes, so will the charge on the associated residue. **(C)** Closed and open states of GLIC. The front-two subunits have been removed and pore hydration is shown in blue. **(D)** Two opposing subunits in the open state. Titratable residues are indicated, with gray corresponding to residues exhibiting a protonation in accordance with the environment pH, orange indicating residues that exhibit a perturbed protonation relative to the environment pH, and green for residues exhibiting state-dependent protonation. Loop C and relevant domain-level changes are also indicated, as well as five residues exhibiting major pH and/or state dependence.

Results

To model state-dependent protonation of GLIC at atomistic level, and demonstrate the applicability of λ-dynamics to this complex pH-gated membrane-protein system, we performed CpHMD simulations of both closed and open structures under resting (pH 7) as well as activating (pH 4) conditions. As a starting model for the closed state, we used the highest-resolution pH-7 structure available, recently determined by cryo-EM to 4.10 Å (PDB ID 6ZGD) [24]. For the open state, we used one of the highest-resolution pH-4 structures, determined by X-ray diffraction to 2.4 Å (PDB ID 4HFI) [10]. Each subunit of the pentameric channel contains 37 Asp, Glu, and His residues, for a total of 185 per receptor, all of which were made titratable. Each GLIC structure was embedded in a homogeneous lipid bilayer, solubilized in 150 mM NaCl, and set to pH 7 or pH 4. For each of the resulting four systems, four 1-µs trajectories were generated. We monitored stability particularly in the ECD, where more than 80% of the titratable residues are located; all trajectories converged within 200 ns (ECD C_α root-mean-square deviation RMSD < 7 Å, Fig. S1). As previously observed [24], deviations were particularly low (ECD C_α RMSD < 4 Å) in simulations of the open state, likely related to the higher resolution and compacted ECD of this starting structure.

Constant-pH MD reveals state-dependent shifts in protonation

To quantify dynamic protonation in GLIC, we calculated time-averaged protonation fractions for each titratable residue across all five subunits and all four replicate simulations of each system. We then classified each residue relative to the predicted protonation fraction for its amino-acid type in solution, as obtained from experimentally reported values [55] and the Henderson-Hasselbalch equation $f_{\text{proto}} = 1/(1 + 10^{\text{pH}-\text{pKa}})$ (Fig. 2A). Fifteen acidic residues (D13 on β1, D55 in the β2-β3 loop, E67 and E69 in the β3–β4 loop, D86

and D91 on β5, E104 on β6, D136 in the β7-β8 loop, D145 and E147 on β8, D154 in the β8–β9 loop, E163 on β9, E222 and E243 at the intracellular mouth of the pore, and H277 on the TMD bottom) fell within 25 percentage points of their predicted solution protonation fractions in all four simulation systems (Fig. S2, gray in 1D, Supplementary Table 1). Notably, all of these residues except E243 were located on aqueous surfaces of the receptor, demonstrating how the CpHMD implementation correctly recapitulates the predicted pH-dependent behavior of solvent-exposed regions.

Conversely, 22 buried acidic residues deviated from the theoretical bulk solution protonation by at least 25 percentage points. Of these, 16 exhibited shifted protonation fractions in both closed and open simulations (Fig. 2B, orange in 1D). For the remaining 6, protonation fractions (additionally) differed between functional states by at least 25 percentage points (Fig. 2C, green in 1D). Shifted protonation fractions could be broadly rationalized by contact analysis. Residues with an elevated propensity to protonate (E26 on β1; E35 in the β1–β2 loop; D122 in the β6–β7 loop; D161 on β9; D178, E181, and D185 on β10; E272 and E282 in the TMD) were typically located in the protein interior surrounded by hydrophobic and/or electronegative atoms, environments that favor protonation of acidic residues (Supplementary Table 1). Although protonation propensity was not heavily state-dependent, specific interactions varied by state. Five such sites are described in detail in the next section.

Asp and Glu residues with a low propensity to protonate (E14 on β1, D31 and D32 in the β1–β2 loop, D49 in the β2–β3 loop, E75 and E82 on β4, D88 on β5, D97 in the β5–β6 loop, D115 in the β6–β7 loop, and D153 in the β8–β9 loop) were frequently proximal to one or more basic Arg or Lys residues (Supplementary Table 1), an environment predicted to favor their deprotonated state. Of the six residues showing signs of state dependence (Fig. 2C), D97 was so poorly resolved in the closed state experimental structure that even the backbone atoms could not be confidently built [24], limiting confidence in state-dependent comparison.

Despite their complex treatment in CpHMD (due to multiple titratable sites), the three His residues in each subunit converged to distinct protonation profiles, again attributable to local environment (Supplementary Table 1). In the ECD, H127 on β7 was partially burried, and exhibited protonation fractions within 26 percentage points of solution predictions (Fig. S2). In contrast, H235 was buried deep within each TMD subunit, and did not sample the doubly protonated state (Fig. 2B). Near the intracellular mouth of the pore, H277 was largely solvent-exposed, and exhibited protonation fractions within 25 percentage points of solution predictions (Fig. S2).

Protonation-dependent rearrangements implicated in gating

To further develop testable hypotheses for GLIC proton gating based on CpHMD, we characterized the dynamic contacts of several titratable residues in detail (Fig. 3A). We first focused on residues E26 and E35, which exhibited a high but submaximal propensity to protonate even at neutral pH, suggesting an early rearrangement in the proton-stimulated conformational wave (Fig. 2B). The other highly protonation-sensitive Glu, E272, was more deeply buried between the TMD interior and lipid bilayer, and did not exhibit pH-dependent dynamics. At E26 on β1, protonation was particularly elevated in open simulations, indicating the protonated form of this residue could selectively stabilize the open state (Fig. 3B). Indeed, although this side chain made relatively few contacts at neutral pH, its protonated form could donate a hydrogen bond to backbone carbonyl atoms of V79 or V81 in the β4–β5 loop of the principal subunit (Fig. 3C–E). The resulting intersubunit interaction could promote compacting, twisting motions of the ECD previously implicated in pLGIC gating, as detailed in the next section.

Residue E35 exhibited even greater protonation propensity than E26 in the closed state (Fig. 3B), consistent with previous reports that it is an initiating proton sensor [23]. Although state dependence of protonation at this position was limited, polar contacts of E35 with the backbone of L114 in the β6–β7 loop, and with T158 in the β8–β9 loop of the complementary subunit, were modestly increased in the open state (Fig. 3C–E). These interactions would favor contraction of the β1–β2 loop towards β6–β7 and the complementary β8–β9, opposing the β-expansion previously associated with pLGIC closure [22]. These results were also broadly consistent with previous fixed-protonation simulations showing rearrangements of E35 in open versus closed GLIC [24], though under CpHMD interactions with L114 were favored over those with T158 or sodium ions (Fig. 3C).

In contrast to these putative early protonation sites, residue E82 in β4–β5 exhibited a state-dependent reduced propensity for protonation, specifically in the closed state at pH 4 (Fig. 3B). Once transitioned to

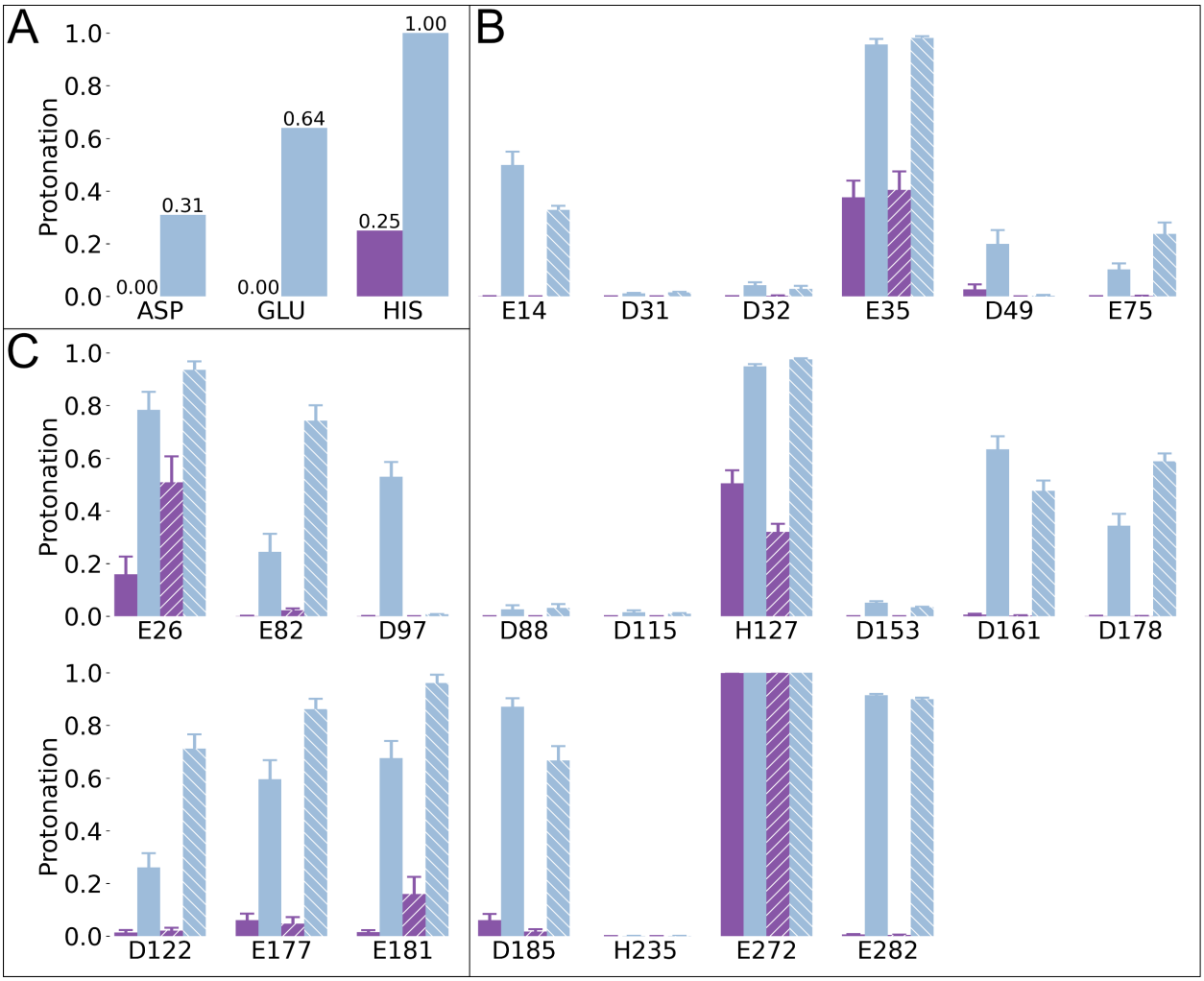

Figure 2: CpHMD reveals state-dependent shifts in protonation. For each titratable residue, mean protonations are provided for both the closed (solid) and open (striped) states at both pH 7.0 (purple) and pH 4.0 (blue), with error bars indicating the standard error estimate. **(A)** Predicted protonation fractions for Asp (pKa 3.65), Glu (pKa 4.25), and His (pKa 6.52) at resting and activating pH, as calculated from the Henderson-Hasselbalch equation. **(B)** Residues exhibiting mean protonations that deviate more than 25 percentage points from the predicted protonation fraction. **(C)** Residues (additionally) exhibiting state dependence, defined as a difference of more than 25 percentage points between the mean protonations in the open and closed state in simulations at the same pH.

the open state, this residue is predicted to fully protonate. Indeed, the closed state favors a salt bridge between the deprotonated form of this residue and K38 on β2 of the complementary subunit (Fig. 3C–E). In the open state, rearrangements in this region bring E82 in closer proximity to T36 on β2 of the same subunit, an interaction that favors the protonated rather than deprotonated side chain. Similar to E35, these contacts would oppose β-expansion, instead favoring compaction of β2 towards β4–β5 within a single subunit.

Interestingly, most acidic residues on β10 (E177, E181, D185) exhibited elevated protonation propensities in the low-pH open state (Fig. 2C). Although this region has not been heavily implicated in GLIC gating, it comprises one strand of Loop C, a critical element that determines neurotransmitter binding to eukaryotic pLGICs [21]. Increased protonation is consistent with closure of β10 over the subunit interface, burying these side chains in a relatively non-polar or electronegative environment in the open state. At the N-terminus of β10, i.e. the tip of Loop C, E177 made a persistent electrostatic contact with R179 on the same strand in the closed state (Fig. 3C–D). In the open state, with the loop relatively closed over the subunit cleft, E177 interacted instead with the backbone of K148 on the complementary β8 strand (Fig. 3C, E). Similar to E26,

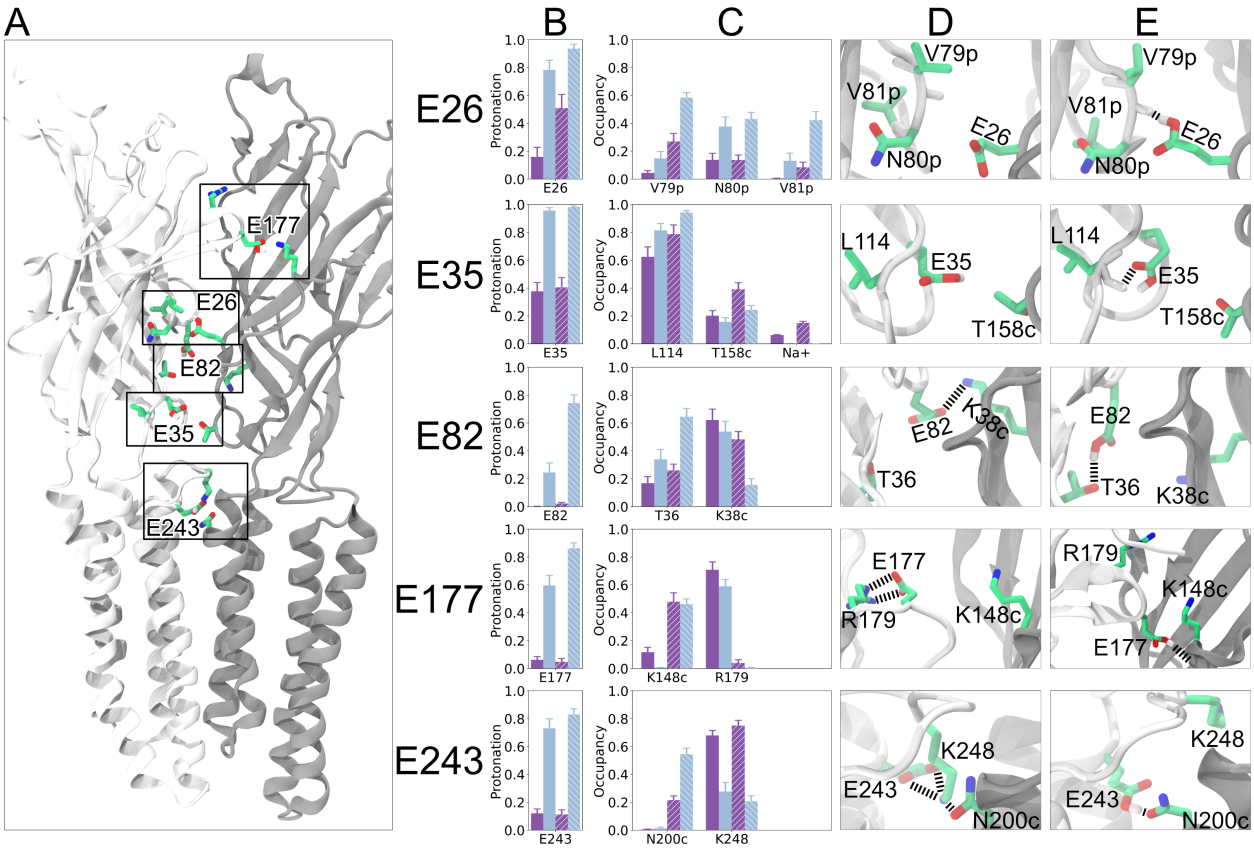

Figure 3: Protonation-dependent rearrangements implicated in gating. This figure shows side chain rearrangements for five residues exhibiting considerable pH and/or state dependence. **(A)** Two opposing subunits shown from the outside of the channel, illustrating the location of residues E26, E35, E82, E177, and E243. **(B, C)** Mean protonation of the titratable residue shown in Fig. 2B **(B)** and H-bond occupancy of relevant contact partners **(C)**. Data is provided for both the closed (solid) and open (striped) states at both pH 7.0 (purple) and pH 4.0 (blue), with the error bars representing standard error estimates. **(D, E)** Schematics (sticks, colored by heteroatom with dashed black lines corresponding to H-bonds) highlighting spatial differences in contact between the closed state at pH 7.0 **(D)** and the open state at pH 4.0 **(E)**.

this rearrangement is expected to promote twisting of the ECD with respect to the TMD.

The M2 residue E243, located at the outer mouth of the transmembrane pore, has also been proposed to influence pH gating. Our simulations indicated a high propensity for protonation of E243 at low pH, particularly in the open state (Fig. 3B). Consistent with previous reports [24], at neutral pH E243 was largely involved in a salt bridge with K248 on the M2–M3 loop (Fig. 3C–D). At low pH, the neutralized E243 interacted more readily with M1 residue N200 from the complementary subunit (Fig. 3C, E). The latter interaction is only favorable after opening of the channel pore, bringing M2 in close proximity to the complementary M1.

Domain-level changes captured by CpHMD

To quantify global as well as local rearrangements captured by CpHMD, we monitored geometric properties of GLIC during simulations of each system. Following conventions of previous computational studies [22, 25], we measured four large-scale changes associated with activation. ECD twist refers to the counter-clockwise rotation of the ECD relative to the TMD, and is expected to assume less negative values during activation (Fig. 4A, left). β-expansion refers to the distance between the β1–β2 and pre-M1 loops, and is expected to decrease (Fig. 4B, left). M2–M1(-) distance is measured between outward-facing ends of the M2 and M1 helices from adjacent subunits, and also decreases with activation (Fig. 4C, left). The 9' radius indicates the capacity of the permeability filter, and is expected to rise (Fig. 4D, left).

ECD properties recapitulated experimental data: simulations in the closed state exhibited more negative

values of ECD twist, and more positive values of β-expansion, with the open state at low pH producing the smallest absolute values (Fig. 4, center). Our simulations also sampled values of both variables corresponding to the initial experimental structures (Fig. 4, right), though the distributions were centered around larger absolute values, indicating a preponderance of closed-like states. The open state at low pH gave a sharper distribution of β-expansion values compared to other systems, indicating a relatively discrete population.

TMD properties also suggested early stages of gating, indicating CpHMD simulations are capable of modeling the initiation of the complex process, although simulating complete transitions will (unsurprisingly) require longer sampling. The open state was associated with a decrease in M2–M1(-) distance and increase in 9' radius (Fig. 4, center). However, values comparable to the experimental open state were not frequently sampled (Fig. 4, right). For M2–M1(-) distance, simulations in the closed state gave sharper distributions, with open-state simulations sampling closed- as well as open-like values. For 9' radius, distributions from all systems were substantially shifted towards smaller values, indicating a tendency towards hydrophobic collapse in the channel pore as previously reported [17].

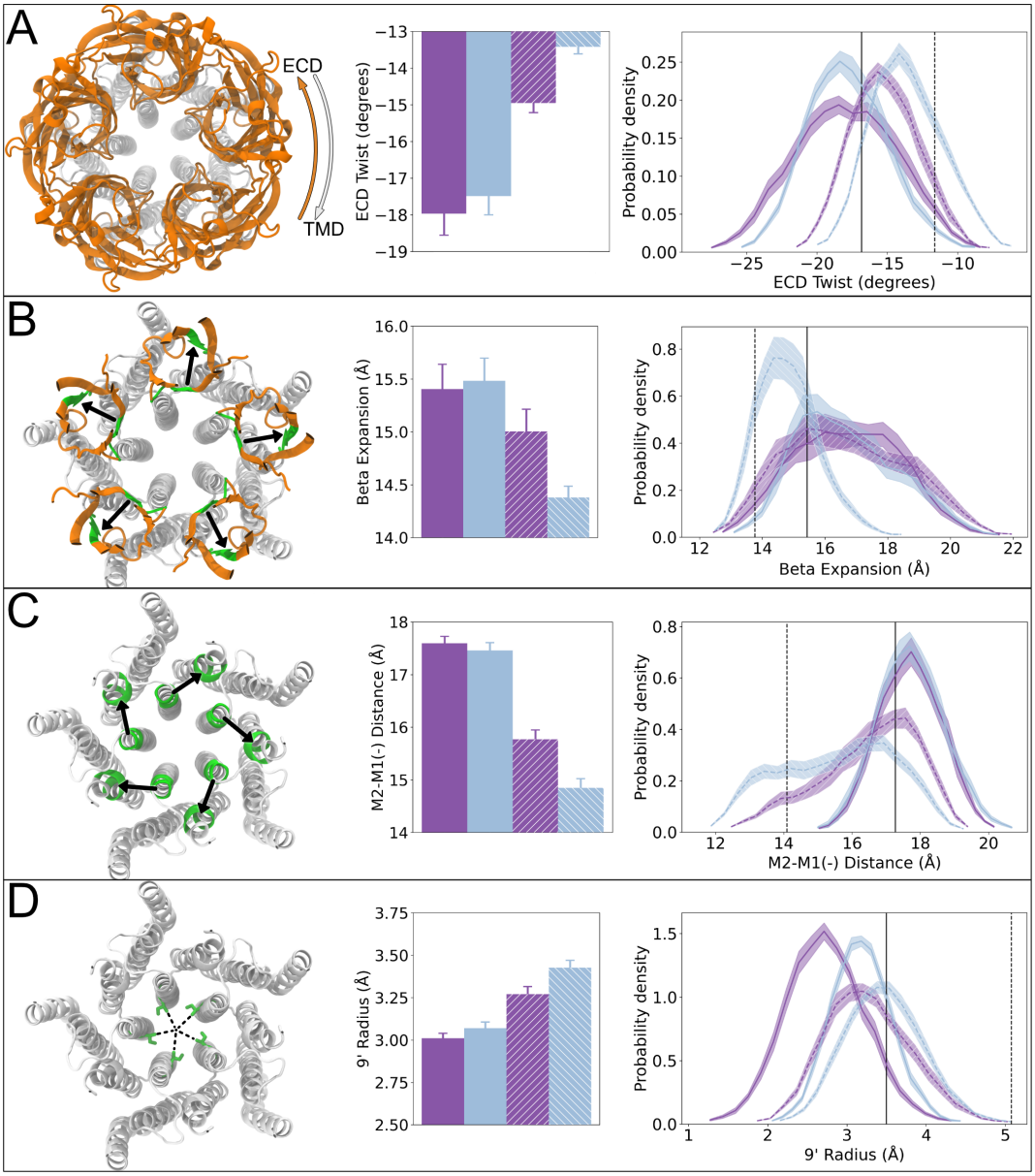

Figure 4: Domain-level changes captured by CpHMD. Four metrics relevant to GLIC gating are shown. For each metric, a motion schematic is provided, with white corresponding to the TMD, orange illustrating the ECD, and green a region of interest. For each metric, mean values and distributions are provided for both the closed (solid) and open (striped) states at both pH 7.0 (purple) and pH 4.0 (blue), with the error bars corresponding to standard error estimates. In the distribution plots, the vertical black solid and dashed lines correspond to the open X-ray (4HFI) and closed cryo-EM (6ZGD) structures, respectively. **(A)** The counter-clockwise twist of ECD relative to the TMD becomes less negative when moving from closed to open states. **(B)** The β-expansion decreases when moving from closed to open states. **(C)** The M2-M1(-) distance decreases from closed to open states. **(D)** The radius at the 9' position/permeability filter increases from closed to open states.

Discussion

Although MD simulations are able to reproduce many types of molecular interactions with good accuracy, they do not typically capture pH-dependence dynamically. Instead, the protonation states of titratable residues are usually set at the start of the simulation and remain fixed during the run, no matter the changes in the local environment of such residues. CpHMD has made promising progress to address this issue, but technical limitations have previously made it challenging to apply to systems as complex as

GLIC due to the large number of titratable residues involved and subtle shifts in protonation. The recent GROMACS λ-dynamics CpHMD implementation made it possible to model the early stages of GLIC pH gating including fully dynamic protonation of all 185 Asp, Glu, and His residues, while also fast enough to generate a total of 16 µs of sampling. This required roughly 45 days, using four nodes each containing four Nvidia Geforce RTX 2080 GPUs. Despite the system size and number of titratable sites, performance was only diminished by approximately 35% compared to classical MD [50], demonstrating the feasibility of the method with contemporary computational resources. Furthermore, although complete gating was not observed (nor expected) at these simulation time scales, we were able to capture both pH- and state-dependent shifts in protonation and domain-level rearrangements in line with the early stages of gating. One interesting challenge in our simulations was the tendency of the pore to collapse. This has been observed in previous MD studies of membrane proteins using the CHARMM force field [17], and might require force field modifications to rectify. All in all, our results corroborated experimental data, emphasizing the accuracy of the implementation and how the simulations pinpoint early molecular determinants of GLIC gating.

A sampling difficulty encountered during the CpHMD simulations was optimizing the height of the bias potential for different titratable groups. As described in [50], one of the four potentials applied to the λ-coordinates is a bias potential. The purpose of this is to limit sampling of the unphysical $\lambda \neq 0, 1$ states as much as possible, while still allowing transitions. By default, the height of this potential is 7.5 kJ/mol. In some cases, mainly buried residues engaging in many electrostatic contacts, it was however observed that these default values were not large enough to prevent sampling of the intermediate λ-states; given the limited maturity of the methods, it is advisable to perform test simulations and adjust barriers before CpHMD production runs. Alternatively, automatic barrier height update schemes could provide a future solution.

Excluding E272, which is buried in the TMD and persistently protonated, E26 and E35 exhibited the largest propensities to protonate at neutral pH out of all residues (Fig. 2). This observation would suggest roles for E26 and E35 as (early) proton sensors in the GLIC gating cascade. Indeed, both E26 and E35 were previously shown to be protonated at low pH [22], with E26 predicted to change protonation upon gating [23] and substitutions to Gln or Ala markedly reducing function [21]. In our simulations, protonation of E26 was associated with increased intersubunit contact with the backbone of V79, N80, and V81 (Fig. 3), possibly facilitating ECD twisting (Fig. 4A), an early domain-level transition in GLIC gating [22]. Furthermore, E35 has been implicated as a key proton-sensing residue in GLIC [23], with its mutation resulting in prominent effects on gating function [21]. This residue, potentially in tandem with the D32-R192-D122 electrostatic triad, could contribute to signal transduction, although the specific role of the triad is not entirely understood. Our simulations show a pronounced pH-dependence for E35, with less influence observed from the state (Fig. 3). Furthermore, a slight increase in intrasubunit contact with L114 was observed in the open state and at low pH, which may correspond to a decrease in β-expansion.

Although our results indicate that E82 and E243 are less likely to protonate (at neutral pH) compared to E26 and E35, they both showed state dependence in their protonation and/or contact partners. E82 is located at the bottom of the vestibular loop and is predicted to protonate at low pH [22]. Our data indicate that E82 tends to release the intersubunit contact with K38 in the open state, and instead prefers to engage with T36 in the same subunit. It is possible that release of K38 thereby contributes to both ECD twisting and a decrease in β-expansion. E243, which marks the extracellular entrance of the TMD, also exhibited state-dependent interaction preferences with nearby polar residues (Fig. 3). When pH is lowered, protonation of E243 weakens its interaction with neighboring residue K248. No longer locked in a salt bridge, both residues are able to rotate more freely, reducing steric clashes (as K248 is no longer pointed downward in between) and allowing E243 to contact N200c on the next subunit (Fig. 3E). This contact could stabilize intersubunit M1–M2 interactions (Fig. 4C) and promote pore opening. Interestingly, E243 was previously shown to maintain M2 helix stability [23], and L248 was shown to reorient between neutral- and low-pH cryo-EM structures [24].

Loop C residues E177, D178, E181, and D185 all showed an increased protonation or state dependence on pH (Fig. 2), with E177 especially showing state-dependent contacts (Fig. 3). E177 is predicted to change protonation upon gating [23] and is believed to help keep the channel open at neutral pH by opposing ECD spreading [22]. Loop C plays an important role in neurotransmitter binding in eukaryotic homologs [21], and our simulations suggest its stabilization is associated with opening, as the stabilizing E177-K148c contact is made almost exclusively in the open state. Thus, pH sensing in GLIC may involve an evolutionary

simpler form of classical ligand binding, nonetheless mediated by a common structural motif. Given that pH sensitivity is not limited to GLIC or to ion channels in general, we anticipate that CpHMD simulations will offer a compelling avenue for investigating a variety of complex proteins in the future.

Materials and methods

System setup

Both closed (PDB ID: 6ZGD [24]) and open (PDB ID: 4HFI [10]) GLIC structures were used as starting models. For 6ZGD, missing side chains were generated using the WHAT IF server [56]. 6ZGD was embedded in a bilayer of 489 1-palmitoyl-2-oleoylphosphatidylcholine (POPC) lipids while 4HFI was embedded in a bilayer of 498 POPC lipids. Both embedding and subsequent solvation in a $14 \times 14 \times 15$ nm^3 box were performed using the CHARMM-GUI membrane builder [57].

The CHARMM36-mar2019-cphmd force field [58] was used in combination with the CHARMM TIP3P water model for topology generation. Here, cphmd signifies the inclusion of CpHMD-specific modifications of bonded parameters for titratable residues. Details on these modifications are described in [51]. The phbuilder tool [59] was used to further prepare the CpHMD simulation inputs for GROMACS: all Asp, Glu, and His residues were made titratable. NaCl was added to neutralize the system (at $t = 0$) and ensure an ion concentration of 150 mM, and 185 buffer particles were added to absorb charge fluctuations and maintain a net-neutral system during the simulations (at $t > 0$). For details on the buffer particles, see [50, 60]. Finally, phbuilder was used to generate all CpHMD-specific input parameters.

CpHMD simulations

All CpHMD simulations were run using the GROMACS CpHMD beta. This version is based on the 2021 release branch and modified to include the routines required for performing the λ-dynamics calculations. The source code branch is maintained at `https://www.gitlab.com/gromacs-constantph` until it has been fully integrated in the main distribution.

Energy minimization of the systems was performed using the steepest-descent algorithm. The first relaxation was performed in the NVT ensemble for 10 ps with a time step of 0.2 fs, using the v-rescale thermostat [61] (coupling time 0.5 ps) and a temperature of 300 K. Bond lengths were constrained using the P-LINCS algorithm [62], and electrostatics performed using the PME method [63]. Subsequent relaxation and production runs were performed in the NPT ensemble using a time step of 2 fs, with pressure kept at 1 bar using the c-rescale [64] barostat (coupling time 5 ps). 30 ns of additional relaxation was performed while gradually releasing restraints on the heavy atoms.

To check whether the default bias potential barriers (7.5 kJ/mol) sufficiently limited sampling of the unphysical $\lambda \neq 0, 1$ states, 20 ns test runs were performed. A number of affected residues were identified, and the inverse Boltzmann method was used to determine the increased barrier height required for those residues. For 4HFI, these included E104 (17.5 kJ/mol), D122 (17.5 kJ/mol), E181 (17.5 kJ/mol), D185 (15 kJ/mol), and E243 (12.5 kJ/mol). For 6ZGD, these included E26 (17.5 kJ/mol), D122 (12.5 kJ/mol), E181 (12.5 kJ/mol), D185 (15), E243 (12.5 kJ/mol), and E272 (15 kJ/mol).

Analysis

Protonation fraction and contact occupancy were computed as the time-average over all five subunits in all four replicas. Cutoffs for the λ-coordinates to constitute a protonated or deprotonated state were set at $\lambda < 0.2$ and $\lambda > 0.8$, respectively. Contact analysis of the acidic residues was performed between either the carboxyl oxygens (Asp, Glu) or the ring nitrogens (His) and the polar (oxygen, nitrogen) atoms of contacting residues. A contact cutoff of 0.4 nm was used for all interactions. In terms of domain-level changes, all measurements were time averaged over five subunits in four replicas, resulting in bar plots and histograms. The ECD twist was defined as the dihedral angle between the C_α COM of the ECD (residues 1-192) in subunit i, the ECD, the TMD (residues 193 to 315), and the TMD in subunit i. β-expansion was defined as the distance between the C_α COM of residues 30-34 (roughly the β1-β2 loop) and the C_α COM of residue 190-194 (part of pre-M1 loop) in a single subunit. The M2-M1(-) distance was defined as the distance

between the C_α COM of residues 241-245 (top of M2 helix) in subunit i and the C_α COM of residues 200-204 (top of M1 helix) in subunit $i+1$. The 9'-radius was defined as the distance between the closest atom in I233 in *a* subunit with the C_α COM of the I233 residues in *all* subunits. MDAnalysis [65] was used extensively for trajectory analysis, and protein renderings were generated using VMD [66].

Data and software availability

The GROMACS constant-pH beta is available at www.gitlab.com/gromacs-constantph. Trajectory subsets, input files, and analysis scripts are archived at zenodo.org under DOI: https://doi.org/10.5281/zenodo.8364284.

Acknowledgements

This research was supported by the Swedish Research Council (grants 2019-04477, 2019-02433, 2021-05806) and the BioExcel CoE (Grant No. H2020-INFRAEDI-02-2018-823830 and EuroHPC 101093290). Computational resources where provided by SNIC (Grants No. 2022/3-40 and 2022/21-16). We also thank Pavel Buslaev for constructive support during the project.

Author contributions

Conceptualization: AJ, PB, EL, RJH; Methodology: AJ, PB; Investigation: AJ; data curation: AJ, RJH; Writing - original draft: AJ, RJH; Writing - review and editing: AJ, PB, RJH, BH, EL; Funding acquisition: BH, EL; Supervision: RJH, BH, EL.

Competing interests

The authors declare no competing interest.

References

[1] Asba Tasneem, Lakshminarayan M. Iyer, Eric Jakobsson, and L. Aravind. Identification of the prokaryotic ligand-gated ion channels and their implications for the mechanisms and origins of animal cys-loop ion channels. *Genome Biology*, 6:R4 – R4, 2004.

[2] Ákos Nemecz, Marie S. Prevost, Anaïs Menny, and Pierre-Jean Corringer. Emerging molecular mechanisms of signal transduction in pentameric ligand-gated ion channels. *Neuron*, 90(3):452–470, 2016.

[3] Ameer N. Thompson, David J. Posson, Pirooz V. Parsa, and Crina M. Nimigean. Molecular mechanism of ph sensing in kcsa potassium channels. *PNAS*, 105(19):6900–6905, 2008.

[4] Pierre Jean Corringer, Marc Baaden, Nicolas Bocquet, Marc Delarue, Virginie Dufresne, Hugues Nury, Marie Prevost, and Catherine Van Renterghem. Atomic structure and dynamics of pentameric ligand-gated ion channels: New insight from bacterial homologues. *Journal of Physiology*, 588:565–572, 2 2010.

[5] Ricarda J C Hilf, Carlo Bertozzi, Iwan Zimmermann, Alwin Reiter, Dirk Trauner, and Raimund Dutzler. Structural basis of open channel block in a prokaryotic pentameric ligand-gated ion channel. *Nature Structural and Molecular Biology*, 17(11):1330–1336, October 2010.

[6] Hugues Nury, Catherine Van Renterghem, Yun Weng, Alphonso Tran, Marc Baaden, Virginie Dufresne, Jean Pierre Changeux, James M. Sonner, Marc Delarue, and Pierre Jean Corringer. X-ray structures of general anaesthetics bound to a pentameric ligand-gated ion channel. *Nature*, 469(7330):428–431, 2011.

[7] Jianjun Pan, Qiang Chen, Dan Willenbring, David Mowrey, Xiang-Peng Kong, Aina Cohen, Christopher B. Divito, Yan Xu, and Pei Tang. Structure of the pentameric ligand-gated ion channel GLIC bound with anesthetic ketamine. *Structure*, 20(9):1463–1469, September 2012.

[8] David Mowrey, Qiang Chen, Yuhe Liang, Jie Liang, Yan Xu, and Pei Tang. Signal transduction pathways in the pentameric ligand-gated ion channels. *PLoS ONE*, 8(5):e64326, May 2013.

[9] Ludovic Sauguet, Rebecca J. Howard, Laurie Malherbe, Ui S. Lee, Pierre-Jean Corringer, R. Adron Harris, and Marc Delarue. Structural basis for potentiation by alcohols and anaesthetics in a ligand-gated ion channel. *Nature Communications*, 4(1), April 2013.

[10] Ludovic Sauguet, Frédéric Poitevin, Samuel Murail, Catherine Van Renterghem, Gustavo Moraga-Cid, Laurie Malherbe, Andrew W. Thompson, Patrice Koehl, Pierre Jean Corringer, Marc Baaden, and Marc Delarue. Structural basis for ion permeation mechanism in pentameric ligand-gated ion channels. *EMBO Journal*, 32(5):728–741, 2013.

[11] Zaineb Fourati, Ludovic Sauguet, and Marc Delarue. Genuine open form of the pentameric ligand-gated ion channel GLIC. *Acta Crystallographica Section D Biological Crystallography*, 71(3):454–460, February 2015.

[12] Ludovic Sauguet, Zeineb Fourati, Thierry Prangé, Marc Delarue, and Nathalie Colloc'h. Structural basis for xenon inhibition in a cationic pentameric ligand-gated ion channel. *PLOS ONE*, 11(2):e0149795, February 2016.

[13] Benoist Laurent, Samuel Murail, Azadeh Shahsavar, Ludovic Sauguet, Marc Delarue, and Marc Baaden. Sites of Anesthetic Inhibitory Action on a Cationic Ligand-Gated Ion Channel. *Structure*, 24(4):595–605, 2016.

[14] Giovanni Gonzalez-Gutierrez, Yuhang Wang, Gisela D. Cymes, Emad Tajkhorshid, and Claudio Grosman. Chasing the open-state structure of pentameric ligand-gated ion channels. *Journal of General Physiology*, 149(12):1119–1138, October 2017.

[15] Zaineb Fourati, Rebecca J. Howard, Stephanie A. Heusser, Haidai Hu, Reinis R. Ruza, Ludovic Sauguet, Erik Lindahl, and Marc Delarue. Structural basis for a bimodal allosteric mechanism of general anesthetic modulation in pentameric ligand-gated ion channels. *Cell Reports*, 23(4):993–1004, April 2018.

[16] Zaineb Fourati, Ludovic Sauguet, and Marc Delarue. Structural evidence for the binding of monocarboxylates and dicarboxylates at pharmacologically relevant extracellular sites of a pentameric ligand-gated ion channel. *Acta Crystallographica Section D Structural Biology*, 76(7):668–675, June 2020.

[17] Hugues Nury, Frédéric Poitevin, Catherine Van Renterghem, Jean Pierre Changeux, Pierre Jean Corringer, Marc Delarue, and Marc Baaden. One-microsecond molecular dynamics simulation of channel gating in a nicotinic receptor homologue. *Proceedings of the National Academy of Sciences of the United States of America*, 107(14):6275–6280, 2010.

[18] Mary Hongying Cheng, Rob D. Coalson, and Pei Tang. Molecular dynamics and brownian dynamics investigation of ion permeation and anesthetic halothane effects on a proton-gated ion channel. *Journal of the American Chemical Society*, 132(46):16442–16449, 2010.

[19] Sebastian Fritsch, Ivaylo Ivanov, Hailong Wang, and Xiaolin Cheng. Ion selectivity mechanism in a bacterial pentameric ligand-gated ion channel. *Biophysical Journal*, 100(2):390–398, 2011.

[20] Nicolas Calimet, Manuel Simoes, Jean Pierre Changeux, Martin Karplus, Antoine Taly, and Marco Cecchini. A gating mechanism of pentameric ligand-gated ion channels. *Proceedings of the National Academy of Sciences of the United States of America*, 110(42), 2013.

[21] Ákos Nemecz, Haidai Hu, Zaineb Fourati, Catherine Van Renterghem, Marc Delarue, and Pierre Jean Corringer. Full mutational mapping of titratable residues helps to identify proton-sensors involved in the control of channel gating in the Gloeobacter violaceus pentameric ligand-gated ion channel. *PLoS Biology*, 15(12):1–22, 2017.

[22] Bogdan Lev, Samuel Murail, Frédéric Poitevin, Brett A. Cromer, Marc Baaden, Marc Delarue, and Toby W. Allen. String method solution of the gating pathways for a pentameric ligand-gated ion channel. *Proceedings of the National Academy of Sciences of the United States of America*, 114(21):E4158–E4167, 2017.

[23] Haidai Hu, Kenichi Ataka, Anaïs Menny, Zaineb Fourati, Ludovic Sauguet, Pierre Jean Corringer, Patrice Koehl, Joachim Heberle, and Marc Delarue. Electrostatics, proton sensor, and networks governing the gating transition in GLIC, a proton-gated pentameric ion channel. *Proceedings of the National Academy of Sciences of the United States of America*, 115(52):E12172–E12181, 2018.

[24] Urška Rovšnik, Yuxuan Zhuang, Björn O. Forsberg, Marta Carroni, Linnea Yvonnesdotter, Rebecca J. Howard, and Erik Lindahl. Dynamic closed states of a ligand-gated ion channel captured by cryo-EM and simulations. *Life Science Alliance*, 4(8):e202101011, aug 2021.

[25] Cathrine Bergh, Stephanie A. Heusser, Rebecca J. Howard, and Erik Lindahl. Markov state models of proton-and pore-dependent activation in a pentameric ligand-gated ion channel. *eLife*, 10:1–23, 2021.

[26] Tyrel Bryan, Javier M. González, John P. Bacik, Nicholas J. DeNunzio, Clifford J. Unkefer, Tobias E. Schrader, Andreas Ostermann, Debra Dunaway-Mariano, Karen N. Allen, and S. Zoë Fisher. Neutron diffraction studies towards deciphering the protonation state of catalytic residues in the bacterial KDN9P phosphatase. *Acta Crystallographica Section F*, 69(9):1015–1019, Sep 2013.

[27] António M Baptista, Paulo J Martel, and Steffen B Petersen. Simulation of protein conformational freedom as a function of ph: constant-ph molecular dynamics using implicit titration. *Proteins: Structure, Function, and Bioinformatics*, 27(4):523–544, 1997.

[28] António M Baptista, Vitor H Teixeira, and Cláudio M Soares. Constant-p h molecular dynamics using stochastic titration. *The Journal of chemical physics*, 117(9):4184–4200, 2002.

[29] Roland Bürgi, Peter A Kollman, and Wilfred F Van Gunsteren. Simulating proteins at constant ph: An approach combining molecular dynamics and monte carlo simulation. *Proteins: Structure, Function, and Bioinformatics*, 47(4):469–480, 2002.

[30] John Mongan, David A Case, and J Andrew McCammon. Constant ph molecular dynamics in generalized born implicit solvent. *Journal of computational chemistry*, 25(16):2038–2048, 2004.

[31] Yilin Meng and Adrian E Roitberg. Constant ph replica exchange molecular dynamics in biomolecules using a discrete protonation model. *Journal of chemical theory and computation*, 6(4):1401–1412, 2010.

[32] Satoru G Itoh, Ana Damjanović, and Bernard R Brooks. ph replica-exchange method based on discrete protonation states. *Proteins: Structure, Function, and Bioinformatics*, 79(12):3420–3436, 2011.

[33] Jason M Swails, Darrin M York, and Adrian E Roitberg. Constant ph replica exchange molecular dynamics in explicit solvent using discrete protonation states: implementation, testing, and validation. *Journal of chemical theory and computation*, 10(3):1341–1352, 2014.

[34] Jason M Swails and Adrian E Roitberg. Enhancing conformation and protonation state sampling of hen egg white lysozyme using ph replica exchange molecular dynamics. *Journal of chemical theory and computation*, 8(11):4393–4404, 2012.

[35] Ulf Börjesson and Philippe H Hünenberger. Explicit-solvent molecular dynamics simulation at constant p h: methodology and application to small amines. *The Journal of Chemical Physics*, 114(22):9706–9719, 2001.

[36] Michael S Lee, Freddie R Salsbury Jr, and Charles L Brooks III. Constant-ph molecular dynamics using continuous titration coordinates. *Proteins: Structure, Function, and Bioinformatics*, 56(4):738–752, 2004.

[37] Jana Khandogin and Charles L Brooks. Constant ph molecular dynamics with proton tautomerism. *Biophysical journal*, 89(1):141–157, 2005.

[38] Serena Donnini, Florian Tegeler, Gerrit Groenhof, and Helmut Grubmüller. Constant ph molecular dynamics in explicit solvent with λ-dynamics. *Journal of chemical theory and computation*, 7(6):1962–1978, 2011.

[39] Jason A Wallace and Jana K Shen. Continuous constant ph molecular dynamics in explicit solvent with ph-based replica exchange. *Journal of chemical theory and computation*, 7(8):2617–2629, 2011.

[40] Jason A Wallace and Jana K Shen. Charge-leveling and proper treatment of long-range electrostatics in all-atom molecular dynamics at constant ph. *The Journal of Chemical Physics*, 137(18):184105, 2012.

[41] Garrett B Goh, Jennifer L Knight, and Charles L Brooks. Constant ph molecular dynamics simulations of nucleic acids in explicit solvent. *Journal of chemical theory and computation*, 8(1):36–46, 2012.

[42] Wei Chen, Jason A Wallace, Zhi Yue, and Jana K Shen. Introducing titratable water to all-atom molecular dynamics at constant ph. *Biophysical journal*, 105(4):L15–L17, 2013.

[43] Juyong Lee, Benjamin T Miller, Ana Damjanovic, and Bernard R Brooks. Constant ph molecular dynamics in explicit solvent with enveloping distribution sampling and hamiltonian exchange. *Journal of chemical theory and computation*, 10(7):2738–2750, 2014.

[44] Plamen Dobrev, Serena Donnini, Gerrit Groenhof, and Helmut Grubmüller. Accurate three states model for amino acids with two chemically coupled titrating sites in explicit solvent atomistic constant ph simulations and p k a calculations. *Journal of chemical theory and computation*, 13(1):147–160, 2017.

[45] Yandong Huang, Wei Chen, Jason A Wallace, and Jana Shen. All-atom continuous constant ph molecular dynamics with particle mesh ewald and titratable water. *Journal of chemical theory and computation*, 12(11):5411–5421, 2016.

[46] Yandong Huang, Robert C Harris, and Jana Shen. Generalized born based continuous constant ph molecular dynamics in amber: Implementation, benchmarking and analysis. *Journal of chemical information and modeling*, 58(7):1372–1383, 2018.

[47] Robert C Harris and Jana Shen. Gpu-accelerated implementation of continuous constant ph molecular dynamics in amber: p k a predictions with single-ph simulations. *Journal of chemical information and modeling*, 59(11):4821–4832, 2019.

[48] Robert C Harris, Ruibin Liu, and Jana Shen. Predicting reactive cysteines with implicit-solvent-based continuous constant ph molecular dynamics in amber. *Journal of chemical theory and computation*, 16(6):3689–3698, 2020.

[49] Julie A Harris, Ruibin Liu, Vinicius Martins de Oliveira, Erik Antonio Vázquez-Montelongo, Jack A Henderson, and Jana Shen. Gpu-accelerated all-atom particle-mesh ewald continuous constant ph molecular dynamics in amber. *Journal of Chemical Theory and Computation*, 18(12):7510–7527, 2022.

[50] Noora Aho, Pavel Buslaev, Anton Jansen, Paul Bauer, Gerrit Groenhof, and Berk Hess. Scalable Constant pH Molecular Dynamics in GROMACS. *Journal of Chemical Theory and Computation*, 2022.

[51] Pavel Buslaev, Noora Aho, Anton Jansen, Paul Bauer, Berk Hess, and Gerrit Groenhof. Best Practices in Constant pH MD Simulations: Accuracy and Sampling. *Journal of Chemical Theory and Computation*, 2022.

[52] Xianjun Kong and Charles L. Brooks. λ-dynamics: A new approach to free energy calculations. *Journal of Chemical Physics*, 105(6):2414–2423, 1996.

[53] Mark James Abraham, Teemu Murtola, Roland Schulz, Szilárd Páll, Jeremy C. Smith, Berk Hess, and Erik Lindah. Gromacs: High performance molecular simulations through multi-level parallelism from laptops to supercomputers. *SoftwareX*, 1-2:19–25, 9 2015. * GROMACS for methods section.

[54] Jochen S Hub, Bert L de Groot, Helmut Grubmüller, and Gerrit Groenhof. Quantifying artifacts in ewald simulations of inhomogeneous systems with a net charge. *Journal of chemical theory and computation*, 10(1):381–390, 2014.

[55] Richard L Thurlkill, Gerald R Grimsley, J Martin Scholtz, and C Nick Pace. pk values of the ionizable groups of proteins. *Protein science*, 15(5):1214–1218, 2006.

[56] G. Vriend. WHAT IF: A molecular modeling and drug design program. *Journal of Molecular Graphics*, 8(1):52–56, 1990.

[57] Emilia L. Wu, Xi Cheng, Sunhwan Jo, Huan Rui, Kevin C. Song, Eder M. Dávila-Contreras, Yifei Qi, Jumin Lee, Viviana Monje-Galvan, Richard M. Venable, Jeffery B. Klauda, and Wonpil Im. CHARMM-GUI membrane builder toward realistic biological membrane simulations. *Journal of Computational Chemistry*, 35(27):1997–2004, 2014.

[58] Jing Huang and Alexander D. Mackerell. CHARMM36 all-atom additive protein force field: Validation based on comparison to NMR data. *Journal of Computational Chemistry*, 34(25):2135–2145, 2013.

[59] Anton Jansen, Noora Aho, Gerrit Groenhof, Pavel Buslaev, and Berk Hess. phbuilder: a tool for efficiently setting up constant ph molecular dynamics simulations in gromacs. Preprint available on ChemRxiv.

[60] Serena Donnini, R. Thomas Ullmann, Gerrit Groenhof, and Helmut Grubmüller. Charge-Neutral Constant pH Molecular Dynamics Simulations Using a Parsimonious Proton Buffer. *Journal of Chemical Theory and Computation*, 12(3):1040–1051, 2016.

[61] Giovanni Bussi, Davide Donadio, and Michele Parrinello. Canonical sampling through velocity rescaling. *Journal of Chemical Physics*, 126(1), 2007.

[62] Berk Hess. P-LINCS: A parallel linear constraint solver for molecular simulation. *Journal of Chemical Theory and Computation*, 4(1):116–122, 2008.

[63] Ulrich Essmann, Lalith Perera, Max L. Berkowitz, Tom Darden, Hsing Lee, and Lee G. Pedersen. A smooth particle mesh Ewald method. *The Journal of Chemical Physics*, 103(19):8577–8593, 1995.

[64] Mattia Bernetti and Giovanni Bussi. Pressure control using stochastic cell rescaling. *Journal of Chemical Physics*, 153(11), 2020.

[65] Naveen Michaud-Agrawal, Elizabeth J. Denning, Thomas B. Woolf, and Oliver Beckstein. Mdanalysis: A toolkit for the analysis of molecular dynamics simulations. *Journal of Computational Chemistry*, 32:2319–2327, 7 2011. * MDAnalysis for methods section.

[66] William Humphrey, Andrew Dalke, and Klaus Schulten. VMD: Visual Molecular Dynamics. *Journal of molecular graphics*, 14(October 1995):33–38, 1996.